Strain-induced coupling of electrical polarisation and structural defects in $SrMnO_3$ films

Carsten Becher[1], Laura Maurel[2], Ulrich Aschauer[1], Martin Lilienblum[1], César Magén[2,3,4], Dennis Meier[1], Eric Langenberg[2], Morgan Trassin[1], Javier Blasco[4,5], Ingo P. Krug[6], Pedro A. Algarabel[4,5], Nicola A. Spaldin[1], José A. Pardo[2,7] and Manfred Fiebig[1]

[1]Department of Materials, ETH Zürich, Vladimir-Prelog-Weg 5, 8093 Zurich, Switzerland

[2]Instituto de Nanociencia de Aragón, Universidad de Zaragoza, C/ Mariano Esquillor, 50018 Zaragoza, Spain

[3]Fundacion ARAID, María de Luna, 11, planta 1ª, Edificio CEEI Aragón, 50018 Zaragoza, Spain

[4]Departamento de Física de la Materia Condensada, Universidad de Zaragoza, C/ Pedro Cerbuna 12, 50009 Zaragoza, Spain

[5]Instituto de Ciencia de Materiales de Aragón, Universidad de Zaragoza – Consejo Superior de Investigaciones Científicas, C/ Pedro Cerbuna 12, 50009 Zaragoza, Spain

[6]Forschungszentrum Jülich, Peter-Grünberg-Institut (PGI-6), Leo-Brandt-Straße, 52425 Jülich, Germany, currently at: Institut für Optik und Atomare Physik, Hardenbergstraße 36, 10623 Berlin, Germany

[7]Departamento de Ciencia y Tecnología de Materiales y Fluidos, Universidad de Zaragoza, C/ María de Luna 3, 50018 Zaragoza, Spain

Local perturbations in complex oxides such as domain walls[1,2], strain[3,4] and defects[5,6] are of interest because they can modify the conduction or the dielectric and magnetic response and even promote phase transitions. Here we show that the interaction between different types of local perturbations in oxide thin films is an additional source of functionality. Taking $SrMnO_3$ as a model system, we use nonlinear optics to verify the theoretical prediction that strain induces a polar phase, and density functional theory to show that strain simultaneously increases the concentration of oxygen vacancies. These vacancies couple to the polar domain walls where they establish an electrostatic barrier to electron migration. The result

is a state with locally structured room-temperature conductivity consisting of conducting nanosized polar domains encased by insulating domain boundaries, which we resolve using scanning probe microscopy. Our "nanocapacitor" domains can be individually charged, suggesting stable capacitance nanobits with a potential for information storage technology.

At first we verify the occurrence of strain-induced polar order in $SrMnO_3$ thin films. Motivated by the search for novel multiferroic materials, which combine magnetic and ferroelectric orders in the same phase, density functional theory (DFT) predicted the occurrence of ferroelectricity in the perovskite-structure alkaline-earth manganites at larger-than-equilibrium lattice parameters[7,8,9]. For bulk $SrMnO_3$ this prediction was confirmed by partial substitution of Sr by Ba which induces negative chemical pressure and leads to a polar state[10]. According to DFT, epitaxial $SrMnO_3$ films should develop a polarisation along one of the pseudocubic <110> axes under >1% epitaxial tensile strain[8].

20-nm films of single-phase $SrMnO_3$ were grown using pulsed laser deposition on (001)-oriented $(LaAlO_3)_{0.3}(Sr_2AlTaO_6)_{0.7}$ (LSAT) with 1.7% tensile strain (see Methods). We characterised the strain state of the films using scanning transmission electron microscopy (STEM) and X-ray and electron diffraction. Figure 1a shows a cross-sectional STEM image evidencing the high quality of the films on the atomic scale with a sharp $SrMnO_3$/LSAT (001) interface. The reciprocal space map in Fig. 1a verifies that the films are tetragonal and coherently strained. The electron diffraction pattern confirms the epitaxial relationship to the substrate. No secondary phases, such as orthorhombic $SrMnO_{2.5}$ (ref. 11), were detected.

Polar order in the strained $SrMnO_3$ films was verified by second harmonic generation (SHG), i.e., frequency doubling of the probing light wave (see Methods). SHG is a particularly powerful in detecting polar phases because, in the leading order, it occurs only in non-centrosymmetric media. It thus emerges free of background when the inversion symmetry is broken by the formation of a polar state. Temperature-dependent SHG measurements of our $SrMnO_3$ films are presented in Fig. 1b. We find a pronounced SHG response indicating a breaking of inversion symmetry at the ordering temperature T_C = 400 K. The SHG intensity reaches a maximum near 250 K, then decreases to a local minimum around 150 K, before it slightly increases again below 100 K. Thus, the SHG data resemble the temperature profile associated with the polar order in chemically strained bulk $Sr_{0.5}Ba_{0.5}MnO_3$. The relation between polar order and strain is cross-checked by confirming the absence of a SHG signal on a centrosymmetric $SrMnO_3$ polycrystal. Comparison to $Sr_{0.5}Ba_{0.5}MnO_3$ furthermore allows us to associate the decrease of the SHG signal in the strained $SrMnO_3$ films below 250 K to the multiferroic onset of antiferromagnetic order which reduces the spontaneous polarisation[10,12].

In the anisotropy plot in Fig. 1c we present the optical polarisation analysis of the SHG signal obtained on a test area of 0.1 mm^2. We fitted the angular dependence of the SHG signal by assuming a distribution of four polar domain states denoted as P_{1+}, P_{1-}, P_{2+}, P_{2-}. The indices refer to the orientation of the polar axis according to $1_\pm \leftrightarrow \pm[110]$ and $2_\pm \leftrightarrow \pm[\bar{1}10]$, see Fig. 1c. The coincidence of the measured data and the fit is excellent with a fitted ratio $r = P_1/P_2 = 0.53$ in the population of P_1- and P_2-type domain states (r varied between different test areas). In contrast, fits assuming a polarisation along the [100] and [010] directions failed. We conclude that the SHG signal identifies exactly the

strain-induced ⟨110⟩-polarised state in the $SrMnO_3$ films that had remained a prediction by DFT up to now[8].

In Fig. 1d we show the distribution of the polar domains by SHG with a spatial resolution of 1 μm. The SHG image reveals micron-sized stripe-like structures of different brightness with preferred orientations along the [100] and [010] directions, i.e. at 45° to the polarisation. The brightness distribution is generated by constructive or destructive interference of SHG contributions from adjacent domains with different orientation of the polarisation[13].

Next, we used electrostatic force microscopy (EFM) to electrically characterise the polar domains and image them with higher resolution. EFM measures the distribution of fixed and mobile charges by recording, respectively, the Ω and 2Ω responses to a tip voltage of frequency Ω, while scanning the sample in non-contact mode (see supplementary Fig. 6)[14]. Figure 2a shows an EFM(2Ω) image taken at ambient conditions with a lateral resolution of 50 nm. Bright and dark areas indicate regions of high and low conductance. In marked similarity to the SHG domain image, the conductance pattern reveals nanosized arrays oriented along the crystallographic [100] and [010] directions. This suggests that the regions of different conductance in Fig. 2a correspond to the polar domains in the SHG image of Fig. 1d. Temperature-dependent EFM(2Ω) scans confirm this: The EFM contrast in Fig. 3 decreases continuously with increasing temperature and vanishes completely around T_C. The conduction pattern reemerges when the sample is cooled again. In order to quantify the variation of the $SrMnO_3$ conductance, we performed complementary conductive atomic force microscopy (c-AFM) measurements. Figure 2b shows a c-AFM scan that reveals a similar variation of brightness, respectively conductance, as the EFM(2Ω) scan in

Fig. 2a. Current-voltage curves in Fig. 2c show that the current through a dark area (#3) is an order of magnitude smaller than through a bright area (#1).

The large difference in the conductance of the polar domains is striking, given that we find no structural or chemical variations between them. There are only four allowed directions of polarisation, but we observe many degrees of brightness (Fig. 2a). Thus, the conductance of a domain is clearly not determined by its direction of polarisation. We notice, however, a rough correspondence between the size of the domains and their conductance, with larger domains in general being brighter. This correspondence suggests that the domains are electrically isolated, with smaller domains having fewer free charges that can contribute to the EFM(2Ω) response. Reference measurements on metallic patches of different sizes deposited on a glass substrate indeed confirm that the signal brightness depends on the size of the conducting region. We conclude, therefore, that the conducting polar domains are separated by insulating barriers – likely the domain walls – that decouple them electrically.

In order to corroborate this model, we scanned an area of several μm^2 in contact mode with +100 V applied to the AFM tip. Subsequently the region around this area was measured by EFM(Ω). The spatial distribution of brightness shown in Figure 4a provides a measure of the electrostatic potential thus obtained. Within the area exposed to the DC voltage the brightness, and hence the electrostatic potential, is much higher than in the surrounding area because of the carriers deposited by the charging process. This charge pattern is stable for many hours. Closer inspection reveals that the brightness is also increased in regions protruding from the area scanned by the AFM tip, as indicated by the arrows in Fig. 4a. Thus, the charge flows from the tip throughout the

entire area of a domain, including the region not scanned by the tip. It does not, however, cross the apparently insulating domain wall.

We then addressed the timescales at which the individual nanodomains can be charged and discharged. To have a higher temporal and also spatial resolution than with scanning probe microscopy we used low energy electron microscopy (LEEM). Here, the electron probe-beam can be used to charge the surface of an insulating sample and simultaneously probe resulting changes in the surface potential landscape. In agreement with our EFM data different nanodomains in the LEEM images in Figs. 4c and 4d are clearly distinguished by their brightness with sharp transitions in the surface potential between the domains. We see that individual domains can switch their potential state reversibly under an electron beam current of 2 μA. The corresponding charging and discharging occurs in less than 30 ms according to Fig. 4e.

To help interpret our experimental results, we used DFT (see Methods) for elucidating the role of oxygen vacancies and their interaction with the polarisation in strained $SrMnO_3$. Our calculations build directly on the earlier predictions of a polar state in strained $SrMnO_3$ (refs. 8, 9) and on calculations of the strain-dependence of defect formation in the related compound $CaMnO_3$ (ref. 6).

First we calculate the strain dependence of oxygen vacancy formation, and find that tensile epitaxial strain promotes the formation of oxygen vacancies on the equatorial site, with 2% strain increasing the vacancy concentration by one order of magnitude at room temperature, consistent with previously reported off-stoichiometry[15]. Figure 5a shows the environment of such a strain-promoted oxygen vacancy. The isosurface shows the electron density associated with the Mn-e_g defect state that converts the two Mn ions adjacent to the vacancy from Mn^{4+} to Mn^{3+}. Next we determine the tendency of

vacancies to cluster, by comparing the total energies of supercells containing oxygen vacancies that are located either close to or far from each other. We find that it is energetically favorable for the vacancies to form columns along the [001] direction (by 0.18 eV per vacancy) or sheets in (100) or (010) planes (by 0.04 eV per vacancy), but that diagonal pairing along the <110> directions is highly unfavorable. Finally, we calculate the tendency of oxygen vacancies to accumulate at domain walls, and obtain an energy gain of 0.30 eV for a vacancy at a 90° polar wall compared to a site one unit-cell into the domain. From nudged elastic band calculations we determine the barrier for migration between equatorial O vacancy sites to be around 0.4 eV, which still yields a significant mobility around T_C = 400 K[16]. Our calculations therefore suggest an accumulation of oxygen vacancies at the (100) or (010)-oriented domain walls when they form at T_C. An estimate in the Supplement shows that in all our experiments the density of oxygen vacancies is large enough to saturate the domain walls. To determine the influence of this accumulation on the transport properties, we calculate the electrostatic energy barrier introduced by a sheet of oxygen vacancies located at a 90° domain wall. We find that, in comparison to a wall without defects, this introduces a potential barrier of 0.024 eV (Fig. 5b) for a mobile electron, effectively limiting conduction to above room temperature.

Two experimental observations confirm the key role of the oxygen vacancies. The results are depicted in Fig. 3 and detailed in the Supplement. First, we expect that above T_C the vacancies are no longer trapped by domain walls but migrate freely. This is corroborated by the homogeneous distribution of conductance above T_C shown in Fig. 3b. Second, because of the low energy of oxygen vacancies at polar domain walls the vacancies are in turn expected to contribute to the nucleation of such walls at T_C. This is confirmed by post-growth thermal annealing experiments performed in different oxygen

environments. We found that with each decrease of the oxygen partial pressure the local conductance of a film within the domains, measured by c-AFM as in Fig. 2b, increases. This increase can be directly associated to an increased density of oxygen vacancies[17]. Figure 3c shows that this is also associated with a pronounced increase in the density of domain walls. Accordingly, many new domains at different brightness levels are created. Note that if, in turn, the annealing is done such that the c-AFM response, i.e. the vacancy concentration, does not change further, the density of domain walls does not change either. The annealing experiments thus confirm that oxygen vacancies contribute to the nucleation of domain walls as predicted above.

In summary, we observe a pattern of electrically decoupled conducting nanoarrays delimited by insulating walls in strained $SrMnO_3$ thin films. The comparison of EFM/c-AFM conductance maps with SHG imaging measurements probing the polar order shows that the conducting nanoarrays and the polar domains form the same pattern, suggesting that the conducting regions separated by insulating barriers are in fact the polar domains limited by insulating domain walls. Using DFT we argue that the observed behavior can be attributed to oxygen vacancy ordering which thus provides a novel, strain-supported mechanism for obtaining functional oxide interfaces within a compound. In $SrMnO_3$ these walls act as functional interfaces by structuring a pattern of nanocapacitors that can be individually charged and discharged, or store charges for many hours. While this demonstration is still a proof of principle, nanopatterned substrates, which are known to structure ferroelectric growth, can be used to promote two-dimensional periodic arrays of these nanocapacitors. Deterministic charging and discharging of an individually addressed cell within this domain matrix would then become feasible. This could form the basis for a new type of electric bit or camera pixel.

References:

1. Salje, E. K. H. & Zhang, H. L. Domain boundary engineering. *Phase Trans.* **82**, 452-469 (2009).

2. Catalan, G., Seidel, J., Ramesh, R. & Scott, J. F. Domain wall nanoelectronics. *Rev. Mod. Phys.* **84**, 119-156 (2012).

3. Schlom, D. G. *et al.* Strain tuning of ferroelectric thin films. *Annu. Rev. Mater. Res*. **37**, 589-626 (2007).

4. Lee, J. H. *et al.* A strong ferroelectric ferromagnet created by means of spin-lattice coupling. *Nature* **466**, 954-958 (2010).

5. Kalinin, S. V., Johnson, C. Y. & Bonnel, D. A. Domain polarity and temperature induced potential inversion on the $BaTiO_3$ (100) surface. *J. Appl. Phys*. **91**, 3816-3823 (2002).

6. Aschauer, U., Pfenninger, R., Selbach, S. M., Grande, T. & Spaldin, N. A. Strain-controlled oxygen vacancy formation and ordering in $CaMnO_3$. *Phys. Rev. B* **88**, 054111 (2013).

7. Bhattacharjee, S., Bousquet, E. & Ghosez, P. Engineering Multiferroism in $CaMnO_3$. *Phys. Rev. Lett.* 102, 117602 (2009).

8. Lee, J. H. and Rabe, M. K. Epitaxial-Strain-Induced Multiferroicity in $SrMnO_3$ from First Principles. *Phys. Rev. Lett.* **104**, 207204 (2010).

9. Rondinelli, J. M., Eidelson, A. S. & Spaldin, N. A. Non-d^0 Mn-driven ferroelectricity in antiferromagnetic $BaMnO_3$. *Phys. Rev. B* **79**, 205119 (2009).

10. Sakai, H. *et al.* Displacement-type ferroelectricity with off center magnetic ions in perovskite $Sr_{1-x}Ba_xMnO_3$. *Phys. Rev. Lett.* **107**, 137601 (2011).

11. Kobayashi, S. *et al.* Labyrinth-Type domain structure of heteroepitaxial $SrMnO_{2.5}$ film. *Appl. Phys. Lett.* **102**, 231911 (2013).

12. Giovannetti, G., Kumar, S., Ortix, C., Capone, M. & van den Brink, J. Microscopic origin of large negative magnetoelectric coupling in $Sr_{1/2}Ba_{1/2}MnO_3$. *Phys. Rev. Lett.* **109**, 107601 (2012).

13. Fiebig, M., Fröhlich, D., Lottermoser, Th. & Maat, M. Probing of ferroelectric surface and bulk domains in ferroelectric $RMnO_3$ (R=Y, Ho) by second harmonic generation. *Phys. Rev. B* **66**, 144102 (2002).

14. Johann, F., Hoffmann, Á. & Soergel, E. Impact of electrostatic forces in contact-mode scanning force microscopy. *Phys. Rev. B* **81**, 094109 (2010).

15. Rørmark, L., Wiik, K., Stølen, S. & Grande, T. Oxygen stoichiometry and structural properties of $La_{(1-x)}A_xMnO_{3+-\delta}$ (A= Ca or Sr and $0 \leq x \leq 1$). *J. Mater. Chem.* **12**, 1058-1067 (2002).

16. Scheiber, P. *et al*. (Sub)surface mobility of oxygen vacancies at the TiO_2 anatase (101) surface. *Phys. Rev. Lett*. **109**, 136103 (2012).

17. Damjanovic, D. Ferroelectric, dielectric and piezoelectric properties of ferroelectric thin films and ceramics. *Rep. Prog. Phys.* **61**, 1267-1324 (1998).

Acknowledgements: We thank the Helmholtz-Zentrum Berlin for the allocation of synchrotron radiation beamtime and C. M. Schneider for support, as well as A. Weber for providing reference samples for EFM measurements. The authors thank J. Rupp and M. Kubicek for advice on the oxygen vacancy dynamics in oxide films. M.F., D.M. and M.L. acknowledge funding from grant "ETH-06 12-2" and from SNF proposal no. 200021-149192. Financial support from Spanish Ministerio de Economía y Competitividad through projects MAT2011-27553-C02 and MAT2012-38213-C02-01, and from Regional Gobierno de Aragón through project E26 is acknowledged. The TEM, XPS and XRD work has been conducted in the Laboratorio de Microscopías Avanzadas at the Instituto de Nanociencia de Aragón – Universidad de Zaragoza whom the authors thank for offering access to their instruments and expertise.

Contributions: C.B. performed and analyzed the SHG measurements. L.M. grew the samples and characterised them together with C.M., J.B., E.L. and M.T. by XRD and STEM. M.L. and C.B. performed EFM. D.M. and I.P.K. carried out LEEM. U.A. performed the DFT calculations. P.A.A., J.A.P., N.A.S. and M.F. supervised the project.

Competing financial interests: The authors declare no competing financial interests.

Additional information: Supplementary information accompanies this paper at www.nature.com/naturenanotechnology. Reprints and permission information is available online at http://npg.nature.com/reprintsandpermissions/. Correspondence and requests for materials should be addressed to M.F.

Figure 1 | Epitaxy and polar order of strained $SrMnO_3$ films. a, STEM image of a cross section of a 20 nm $SrMnO_3$/LSAT (001) film confirming the atomically sharp interface and the crystalline quality of the perovskite film. Inset: The reciprocal space map obtained by X-ray diffraction (left) evidences coherent tensile strain of 1.7%, and an electron diffraction pattern (right) confirm the coherent growth of the films. Scale bar, 2 nm. **b**, The temperature-dependent normalised SHG intensity reveals the reversible emergence of a noncentrosymmetric phase at 400 K. **c**, SHG polarisation analysis (measurement principle sketched) along with a fit (solid line) assuming, as sketched, a mixture of polar $P_{1\pm}$ and $P_{2\pm}$ domains in the film. **d**, SHG microscopy image of the polar domain structure taken under ambient conditions with a resolution of 1 μm. A pattern of micrometer-sized domain stripes oriented along the [100] and [010] axes is resolved. Scale bar, 5 μm.

Figure 2 | Patterned conductance in strained $SrMnO_3$ films. a, Map of the normalized conductance map of a 20 nm $SrMnO_3$/LSAT (001) film obtained at room temperature on an area of 50×50 μm^2 by EFM(2Ω). The degree of brightness scales with the conductance. Resolution is 50 nm. A distribution of stripe-like nanoarrays as in Fig. 1d is observed. Scale bar, 5 μm. **b**, Conductance map obtained at room temperature on an area of 1.9×2.0 μm^2 by c-AFM. The pattern resembles that in **a**. Scale bar, 0.5 μm. **c**, Current-voltage curves recorded at the positions indicated in **b**. Note that between positions, the local conductance varies within an order of magnitude.

Figure 3 | Temperature dependence of the conductance pattern. a, Comparison between SHG signal and EFM(2Ω) contrast (i.e. difference between brightest and darkest region) as function of temperature, both normalised to their values at 300 K. Error bars show the variance of the measured temperature and EFM contrast. **b**, EFM(2Ω) images of nearby regions taken at different temperatures demonstrate the decrease of contrast towards zero at the transition temperature of 400 K. The brightness scales with the normalized conductance with the same conductance range used in the three images. Scale bar, 0.5 μm. **c**, Maps of the normalised conductance obtained by c-AFM of the same region on a $SrMnO_3$ film before and after annealing at 620 K in 1 bar O_2. Scale bar, 2 μm.

Figure 4 | Polar domains as nanocapacitors. a, Map of the normalised electrostatic potential obtained by EFM(Ω) after scanning the area enclosed by the dashed red line with an AFM tip biased by +100 V. Scale bar, 1 μm. The higher degree of brightness, which corresponds to an increase in the potential, shows that the nanodomains have been charged. Note that the charged area extends beyond the region scanned by the tip, as indicated by the arrows in **a** and sketched in **b.** **c**, LEEM map of the normalised electrostatic potential during charging with the electron beam. Scale bar, 1 μm. **d**, LEEM image of the area in **c**, but taken 30 ms later. The electrostatic potential of the highlighted domain and, correspondingly, the charge deposited into it, has changed abruptly. **e**, Time dependence of the normalised LEEM brightness of this domain showing that under the electron bombardment the charging process is reversible. Error bars show the variance derived from a series of images . Solid line is a guide to the eye.

Figure 5 | Electronic structure calculations of oxygen vacancy formation. a, Part of the simulation cell showing the calculated relaxed crystal structure around an oxygen vacancy in strained polar perovskite $SrMnO_3$. The 0.008 e/Å^3 isosurface (yellow) shows the defect-state electron density located on the two Mn ions next to the vacancy. **b**, Calculated electrostatic potential across a 90° head-tail domain wall without and with an oxygen defect layer. Up to about room temperature, the latter poses an insulating barrier to conduction.

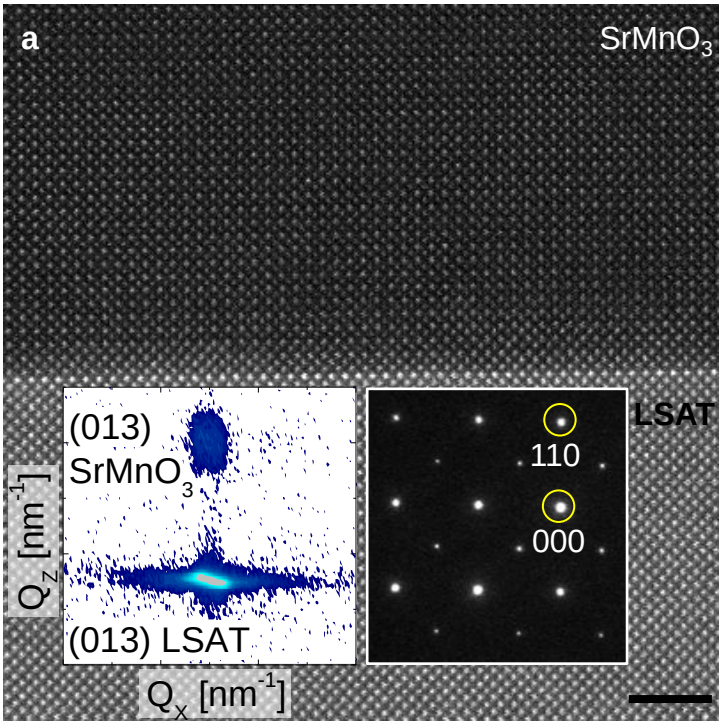
a
SrMnO3
LSAT
(013)
SrMnO3
(013) LSAT
110
000
Qz [nm-1]
Qx [nm-1]

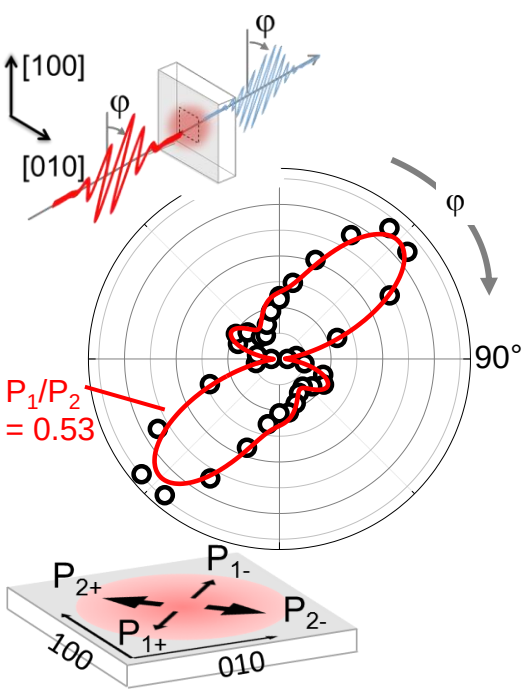
c
[100]
[010]
φ
φ
90°
P1/P2
= 0.53
P1-
P2+
P2-
P1+
100
010

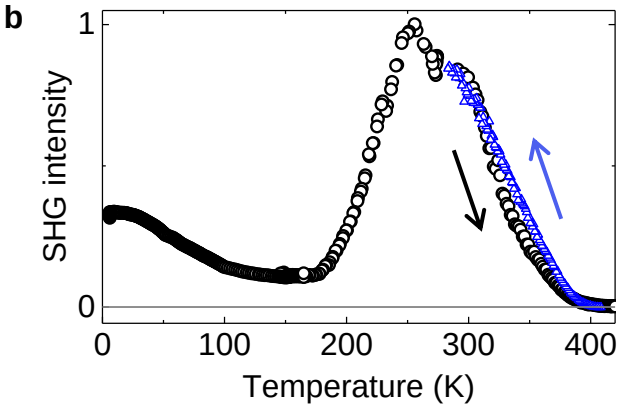
b
SHG intensity
1
0
0
100
200
300
400
Temperature (K)

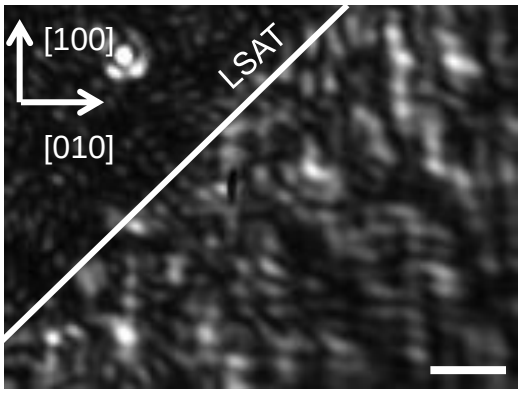
d
[100]
[010]
LSAT

Figure 1

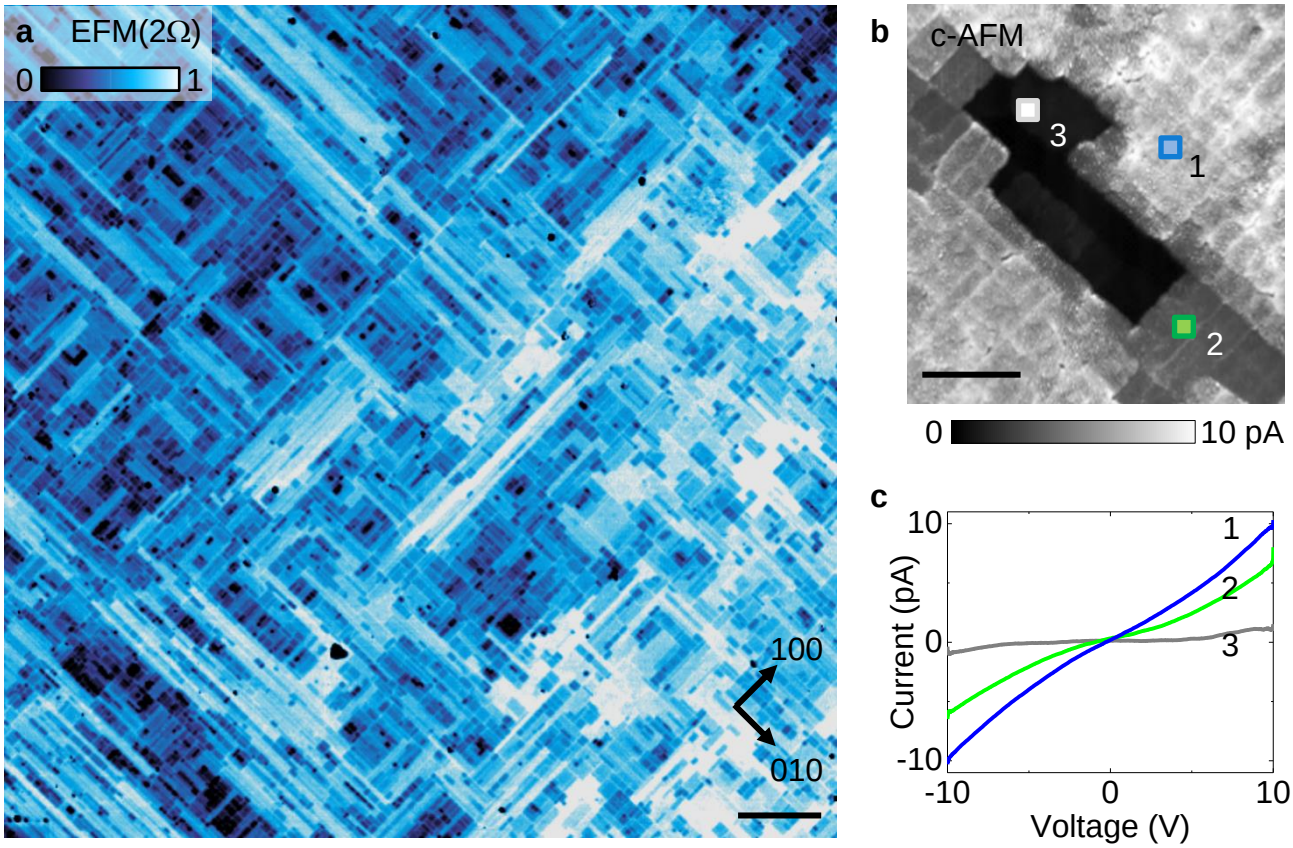
a
EFM(2Ω)
0
1
100
010
b
c-AFM
3
1
2
0
10 pA
c
10
0
-10
Current (pA)
1
2
3
-10
0
10
Voltage (V)

Figure 2

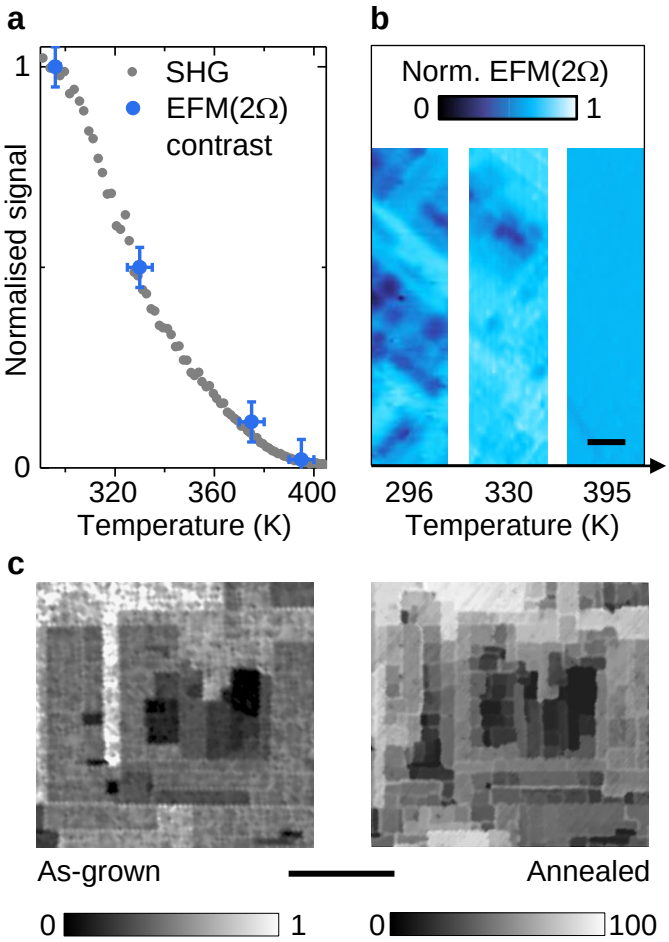
a
b
c
1
0
SHG
EFM(2Ω)
contrast
Normalised signal
320
360
400
Temperature (K)
Norm. EFM(2Ω)
0
1
296
330
395
Temperature (K)
As-grown
Annealed
0
1
0
100

Figure 3

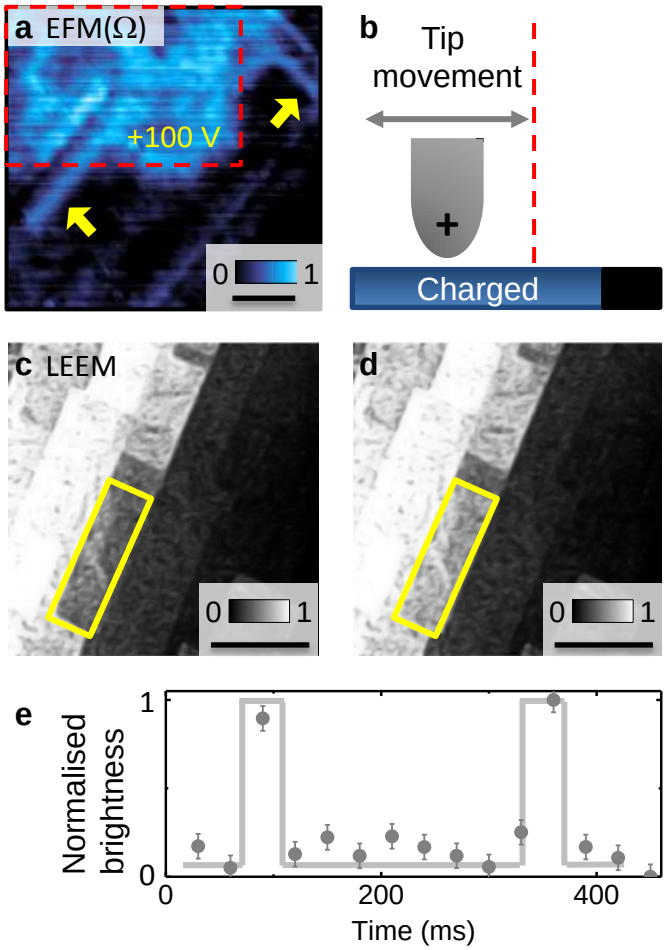
a EFM(Ω)
+100 V
0
1
b
Tip
movement
+
Charged
c LEEM
0
1
d
0
1
e
Normalised
brightness
1
0
0
200
400
Time (ms)

Figure 4

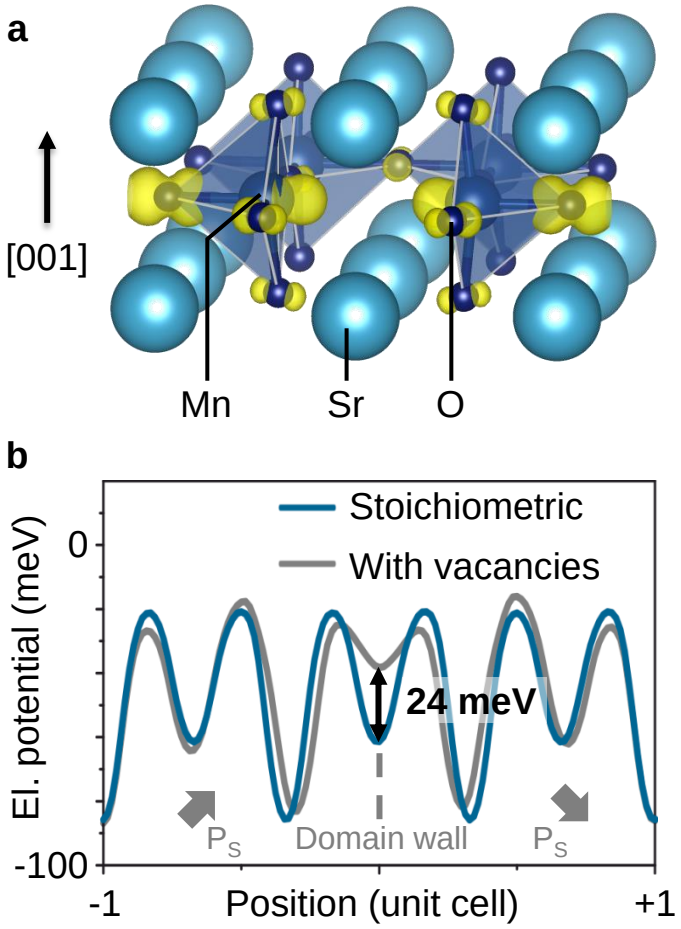
a
[001]
Mn
Sr
O
b
El. potential (meV)
0
-100
Stoichiometric
With vacancies
24 meV
P_S
Domain wall
P_S
-1
Position (unit cell)
+1

Figure 5